Topological classification for intersection singularities of exceptional surfaces in pseudo-Hermitian systems

Hongwei Jia[1,2,#], Ruo-Yang Zhang[1,#], Jing Hu[1], Yixin Xiao[1], Shuang Zhang[3], Yifei Zhu[4,*], C. T. Chan[1,†]

[1]Department of Physics, The Hong Kong University of Science and Technology, Clear Water Bay, Kowloon, Hong Kong, China

[2]Institute for Advanced Study, The Hong Kong University of Science and Technology, Clear Water Bay, Kowloon, Hong Kong, China

[3]Department of Physics, The University of Hong Kong, Pokfulam Road, Hong Kong 999007, China

[4]Department of Mathematics, Southern University of Science and Technology, Shenzhen, Guangdong, China

#These authors contributed equally to this work

Abstract: Non-Hermitian systems exhibit rich topological characteristics that relate to a wealth of exotic physical effects. As such, to fine-tune these systems for optimal device operation or material properties, exceptional points play a crucial role. Notably, they can form exceptional surfaces that afford embedded lower-dimensional non-isolated singularities. In this study, given a generic non-Hermitian system with parity–time and pseudo-Hermitian symmetries, we provide the first topological classification for non-defective intersection lines, i.e., degeneracy lines where exceptional surfaces intersect transversally. Specifically, by constructing the quotient space of an order-parameter space subject to equivalence relations between eigenstates, we reveal that the space of such gapless structures has its fundamental group presented as a non-Abelian free group on three generators. This classification predicts a novel kind of non-Hermitian gapless topological phase that features a chain of non-defective intersection lines in band structures. Moreover, it predicts the existence of topologically protected edge states in one-

dimensional lattice models that originate from intersection singularities. For such gapless phases, these edge states are unexpected from conventional Zak phase theory.

Introduction. Singularities are ubiquitous and play significant roles in various physical systems in the real world, often accompanied by exotic physical phenomena[1–13]. For example, in topological materials, a Weyl point in a Hermitian system acts as a sink or source of the Berry curvature, and two Weyl points with opposite chiralities are connected by a Fermi-arc surface state[1,2,9,11]. The existence and stability of singularities can be better understood via topology, and a singularity can be characterized by a topological invariant, such as the Chern number. This invariant is usually encoded in the adiabatic evolution of eigenstates over closed loops or surfaces that enclose the singularity point[5–9,11]. Recently, the topology of non-Hermitian systems has attracted growing attention[14–25]. As unique features of non-Hermiticity, exceptional points are singular points on the complex energy plane where both the eigenenergies and the eigenstates coalesce[14–19]. They differ from the usual degeneracies of Hermitian systems, such as Weyl points, Dirac points, and nodal lines, in that they may carry fractional topological invariants[16,18,19,24,26] and can induce stable bulk Fermi-arcs[22,24] and braiding of eigenvalues[26]. The non-Hermitian skin effect, manifested by sensitivity of the eigen-spectrum to boundary conditions, is associated with the point gaps in bulk topology[15–18,21,23,25]. Recent discoveries of lines, rings, and surfaces of exceptional points have further enriched the classes of topological degeneracies[27–31]. In particular, high-order exceptional degeneracies, which frequently appear as the cusps of exceptional lines or surfaces, carry a hybrid type of topological invariants in a high-dimensional parameter space[32].

In the meantime, significant efforts have been devoted to classifying these exceptional points and related energy band structures. Topological classifications are of particular importance, as they enable predictions of degeneracies in the parameter space whenever the type of energy gaps and the Altland–Zirnbauer symmetry class of a system are known[14,19,20,33–35]. This provides a theoretical framework for predicting non-Hermitian topological phases of matter and for guiding their experimental realizations. In particular, exceptional points can assemble into hypersurfaces in a 3D parameter space, called exceptional surfaces (ESs), which separate exact and broken phases[20]. ESs are commonly observed in non-Hermitian systems with parity–time inversion (*PT*) symmetry or chiral symmetry[20,27–29] and have broad applications in the design of sensing and absorption devices[31,36]. As a subspace of the parameter space, ESs may possess embedded lower-dimensional singularities, which have remarkable properties differentiating them from other points on the ESs. These so-called hypersurface singularities include intersections[37], cusps[38–40], and swallowtail catastrophes[41]. They are symmetry protected and stable against symmetry-preserving perturbations[31,37–41]. However, despite various important physical phenomena and potential applications, these hypersurface singularities on ESs have never been topologically classified.

In this work, we provide the first topological classification for a typical hypersurface singularity in two-band models where exceptional surfaces intersect transversally. We call it a non-defective intersection line (NIL) of the ESs. An NIL commonly appears in generic non-Hermitian systems with *PT*-symmetry and an additional pseudo-Hermitian symmetry[41]. The band structures of such systems feature a gapless configuration of ESs connected at an embedded NIL. We analyze equivalence relations of eigenstates, and discover that the quotient space of the order-parameter space is homotopy equivalent to a bouquet of three circles $M = S^1 \vee S^1 \vee S^1$. The topology of this NIL is thus characterized by the fundamental group of *M*, which is a non-Abelian free group on three generators. Essentially, we introduce intersection homotopy theory to classify such non-isolated singularities for the first time, which is very different from the usual homotopy theory addressing isolated singularities[6,26,32–35,40]. Our classification systematically explains exotic physical effects arising from the nontrivial topology of NILs, such as the formation and evolution of a chain of NILs. In addition, our topological description predicts the stable edge states in one-dimensional lattice models protected by a topological NIL, even though they are counter-intuitive for gapless phases and go beyond conventional explanations by Zak phase theory.

Main. The prototypical Hamiltonian is a two-level system *H* that is *PT*-symmetric and preserves an additional η-pseudo-Hermitian symmetry[41–43]:

$$[H, PT] = 0, \qquad \eta H \eta^{-1} = H^{\dagger} \tag{1}$$

Here, the operator PT can be regarded as complex conjugation with a suitable choice of basis in parameter space, and thus the Hamiltonian can always be gauged to be real. The metric operator η here takes the Minkowski metric $\eta = \mathrm{diag}(-1,1)$ [13,41,44,45]. More details on pseudo-Hermiticity are provided in Section 1 of Supplementary Information. These symmetries imply that the **k**-space Hamiltonian can be written in the form

$$H(\mathbf{k}) = f_2(\mathbf{k}) i\sigma_2 + f_3(\mathbf{k})\sigma_3 \tag{2}$$

where $f_{2,3}$ are real-valued functions of three-dimensional (3D) **k**-space, and $\sigma_{2,3}$ are Pauli matrices. There is no term multiplied by σ_1 due to the above PT-symmetry. Without loss of generality, we may assume that the term multiplied by the identity matrix vanishes as well, because it does not affect the gapless structure. Such Hamiltonians correspond to physical systems with nonreciprocal hopping of orbitals[41,46–48].

In analogy with the Hermitian case[6], the 2D $f_{2,3}$-plane serves as the order-parameter space of all Hamiltonians that preserve the symmetries specified in Eq. (1). In particular, as $f_{2,3}$ are real functions on **k**-space, any exceptional surfaces (ESs) in the 3D **k**-space correspond to exceptional lines (ELs) at $f_2 = \pm f_3$ on the 2D $f_{2,3}$-plane. The ESs intersect transversally in lines (i.e. the NILs) in the **k**-space, which in turn correspond to the intersecting point (called a non-defective intersection point, or NIP) of the ELs at the origin $f_2 = f_3 = 0$. Moreover, a path traced in the 3D **k**-space maps to a path on the 2D $f_{2,3}$-plane, and if the path loops around an NIL in the **k**-space, the corresponding path in the $f_{2,3}$-plane encircles the NIP. Figure 1a shows the gapless structure of the order-parameter space, with red and green lines representing the ELs satisfying $f_2 = \mp f_3$, respectively. Regions I and III (satisfying $|f_2| < |f_3|$) support Hamiltonians with real eigenenergies and are referred to as PT-exact phases. On the other hand, regions II and IV ($|f_2| > |f_3|$) are PT-broken phases, where the eigenvalues come in complex-conjugate pairs. The paths α, α', β and β' begin and terminate at the ELs, and they are located in different regions (Fig. 1a). We aim to classify the NIP at the origin, which is excluded from the plane[20,49]. First, the plane punctured at the origin deformation retracts to a circle S^1 (Fig. 1b). Such a mathematical process can be interpreted as a quotient map, which identifies all points along each ray starting from the origin (excluding the origin). This identification is based on the equivalence relation that all points on the ray, namely the Hamiltonians, have the same eigenstates ordered by eigenvalues. Consequently, the upper and lower halves of EL_1 shrink to antipodal points A and A', respectively, while those of EL_2 to B and B'. Moreover, there are two equivalence relations on the S^1. At point A, the two eigenstates coalesce, which coincides with the coalesced eigenstates at point A'. Therefore, A and A' should be identified, and one can glue A' to A via a quotient map. The same procedure applies to B and B'. It is important to note that antipodal points located in the regions where eigenenergies are gapped cannot be identified, because their eigenstates are reversely ordered by the eigenenergies. Such a refined topological discrimination of the strata of the origin, the intersecting lines $f_2 = \mp f_3$ and the plane is a distinguished feature of intersection homotopy methods[50,51]. The intersection homotopy method, which is a mathematical technique used to address hypersurface singularities, differs significantly from the conventional homotopy method that focuses on the topology of isolated singularities. In the conventional homotopic loops, the intention is to avoid intersecting singularities[6,49], which inherently makes it incapable of dealing with singularities that are entirely located on ESs (or ELs in 2D), just like our case. When dealing with non-isolated singularities, the parameter space becomes stratified (as described in Section 2 of the Supplementary Information), and the singular hypersurfaces ESs (or ELs in 2D) that satisfy $f_2 = \mp f_3$ form a subspace within the parameter space, known as a stratum. Unlike conventional homotopic loops, the intersection homotopic loops do not need to avoid intersecting this stratum [although intersecting NIL (or NIP in 2D) should be avoided because it is our classification target]. In this context, we can define equivalence relations on ESs (or ELs in 2D). Using the above procedures, we obtain the quotient space of the S^1 in Fig. 1b, which is a bouquet of three circles (see Fig. 1c)

$$M = S^1 \vee S^1 \vee S^1 \tag{3}$$

The notion of quotient space has been widely applied in physics, and the basic technique is gluing identified points within the parameter space under well-defined equivalence relations. A prominent example is the first Brillouin zone, which serves as a quotient space. We know that the band dispersions are repetitive with respect to Brillouin zones. Parameters with interspaces being multiples of reciprocal lattice vectors can thus be identified. Moreover, the first Brillouin zone can be further reduced to a quotient space, such as a circle S^1 (in 1D) or a torus $S^1 \times S^1$ (in 2D), by gluing together points on the Brillouin zone boundary that share the same eigenvalues and eigenstates. Furthermore, the concept of quotient space has been utilized to classify isolated singularities[6]. More detailed mathematical discussions on quotient spaces can be found in Section 2 of the Supplementary Information. The fundamental group of M can be calculated as

$$\pi_1(M) = \mathbf{Z} * \mathbf{Z} * \mathbf{Z} \tag{4}$$

which is a free non-Abelian group on three generators. As shown in Fig. 1c, the three generators Z_1, Z_2 and Z_3 of the group can be given by the concatenations of paths $\alpha\beta$, $\alpha\alpha'^{-1}$ and $\alpha'\beta'$, respectively. These topological invariants associate with the frame deformations of eigenstates along these paths, which are explained in detail in Section 3 of Supplementary Information.

To better understand how this group encodes physical information, we now introduce loops (or concatenated paths) in the order-parameter space that carry nontrivial or trivial topological invariants. The concatenated paths characterizing the generators Z_1, Z_2 and Z_3 are shown in Figs. 2a–c, respectively, where the dashed lines with arrow denote quotient maps that glue identified points. We note that the gluing process does not mean the loop passes through the NIP. Each of the concatenated paths corresponds to an S^1 in Fig. 1c, which are loops in the quotient space M generating its fundamental group. In Fig. 2d, a loop in the plane encircling the NIP is also a concatenation of paths $\alpha\beta\alpha'\beta'$, which carries the topological invariant Z_1Z_3, an element in the group [Eq. (4)]. Some other nontrivial loops are discussed in Section 4 of Supplementary Information. Typical loops carrying the trivial topological invariant are shown in Figs. 2e–g. The loop l does not cut through any EL and is thus confined in a single region, which is always trivial because it cannot enclose any singularity (i.e. the excluded point, NIP). As we transport l upwards past one of the ELs, the loop decomposes into two paths l_1 and l_2 (Fig. 2f). As the endpoints of l_1 (or l_2) can be identified, l_1 (or l_2) becomes a loop in the quotient space M. It is a trivial loop that can shrink to a point without encountering the NIP. Therefore, the concatenation l_1l_2 is also trivial. By further expanding l downwards to cut through the other EL (see Fig. 2g), the loop becomes a product $l_1l_3l_4l_5$. Since both l_1 and l_4 correspond to trivial loops in the quotient space M, this product is equivalent to the concatenation l_3l_5. In addition, paths l_3 and l_5 are along opposite directions and are homotopic to α^{-1} and α, respectively. It is thus not difficult to find out that the product $l_1l_3l_4l_5$ remains trivial. From the above analysis, we conclude that *continuous deformations of a loop (or a path), even encountering ELs (or ESs for 3D), will not change the topology*. In contrast, *encountering NIPs (or NILs for 3D) will change the topology*. Similar conclusions have also been drawn in Ref. 41. Importantly, as can be indicated from the above analysis, a path joining ELs (or ESs) can provide a lot of information on the NIP (see Section 4 of Supplementary Information for adiabatic evolution of eigenstates) even though it appears open in the parameter space, which is substantially different from the situation with isolated singularities. Therefore, if a loop is partitioned into several segments by ELs (or ESs), it is necessary to investigate the evolution of eigenstates along each path before discussing their combined consequence.

Next, based on our topological descriptions, we aim to understand the formation of chain-like structures composed of NILs and their evolution as the Hamiltonian deforms. The chain of singular lines in parameter space is a nontrivial phenomenon which has previously been observed for nodal lines in PT-symmetric Hermitian systems[6]. Here, we show that such an interesting joining phenomenon of singular lines can also occur with NILs, for example,

$$f_2(\mathbf{k}) = k_x k_z, \quad f_3(\mathbf{k}) = -k_x^2 + k_y^2 + k_z^2 - d \tag{5}$$

The Hamiltonian exhibits a chain-like structure in **k**-space as depicted in Fig. 3a1: a circular NIL located on the plane $k_x = 0$ is chained to a pair of hyperbolic NILs located on the plane $k_z = 0$ at two intersecting points. All the NILs (satisfying the equations $f_2 = f_3 = 0$) are contained in ESs, which are represented by the red (ES_1) and green (ES_2) surfaces (satisfying $f_2 = \mp f_3$, respectively) corresponding to EL_1 and EL_2 in Fig. 1, respectively. We begin by examining the loop l_6, which encloses the waists of the two ESs and their NILs, and which does not cut through any of the ESs. According to our previous analysis, such a loop, similar to l (Fig. 2e), is topologically trivial. This may not be immediately apparent from the figure, as the ESs and NILs seem to prevent the loop from retracting to a point. However, by changing d from positive to negative, the waists of the ESs first gradually retract to a point (as shown in Fig. 3b1) and then open up to form a gap (as shown in Fig. 3c1). The two hyperbolic NILs enclosed by the loop in Fig. 3a1 thus annihilate each other, consistent with the topological triviality of l_6. Moreover, the trivial loop l_6 enforces the ESs containing the two NILs to remain smooth as the Hamiltonian deforms. This can be explained by l_6' (see Fig. 3a1), which is homotopic to l_6, as they enclose the same NILs, but l_6' traverses the ESs. On its plane of cross section, as sketched in Fig. 3a2, l_6' is segmented by the ESs into several paths, where the red and green lines denote the traces of ES_1 and ES_2 on that plane. The topological invariants of the segments along l_6' must cancel each other to form a trivial product, which implies that each path l_t, connecting points of a single ES without cutting through the other ES, must carry a trivial topological invariant. This agrees with our previous analysis of l_1, l_2 and l_4 in Fig. 2. As one continues to deform the Hamiltonian ($d < 0$), the two ESs enclosed become disjoint once the two NILs annihilate (see Figs. 3c1–c2). Moving on to the loop l_7 in Fig. 3a1, we see that it is segmented by the ESs into various paths, as depicted in Fig. 3a3. This loop can be represented as a concatenation of paths $(\beta^{-1}\alpha^{-1}\beta'^{-1}\alpha'^{-1})^2$, carrying a nontrivial squared topological invariant $(Z_1^{-1}Z_3^{-1})^2$. This invariant prevents the two encircled circular NILs from annihilating each other as d varies in the Hamiltonian [Eq. (5)]. The two NILs merge to a point when $d = 0$ (Fig. 3b1), dividing the nearby area into eight regions (see Fig. 3b3). Since the loop is still the product $(\beta^{-1}\alpha^{-1}\beta'^{-1}\alpha'^{-1})^2$, its topological invariant does not change and remains to be squared $(Z_1^{-1}Z_3^{-1})^2$. As d varies further, the point splits, and the two NILs become separate in opposite directions, as shown in Figs. 3c1, c3. Thus, the squared invariant $(Z_1^{-1}Z_3^{-1})^2$ is conserved throughout the deformation of this Hamiltonian. *The conservation of the squared invariant* $(Z_1^{-1}Z_3^{-1})^2$ *on* l_7 *and the trivial invariant on* l_6 *(or* l_6'*) is a necessary condition for the chain of NILs.* To observe the chain-like structure of NILs, we can design 3D periodic systems with nonreciprocal hopping between orbitals. The nonreciprocal hopping between orbitals has already been realized in phononic systems and electric circuits with the employment of active devices[41,52]. A design of a 3D face-centered cubic (fcc) lattice model, as well as the hopping parameters between orbitals, are shown in Section 5 of Supplementary Information. We note that the chain-like structure of NILs is protected by the mirror symmetries $k_x \mapsto -k_x$ and $k_z \mapsto -k_z$, and breaking the symmetries will eliminates such a structure. These physical consequences can all be observed based on the design in Section 5 of Supplementary Information. The invariant conservation shows that two inannihilable NILs cannot be directly connected by smooth ESs, as one observes in Figs. 3a3–c3.

Finally, we demonstrate that an NIL (or NIP) can host topologically protected edge states, which represents a whole new type of bulk–edge correspondence that appears in a gapless non-Hermitian system. This concept may seem counterintuitive, as bulk–edge correspondence is typically discussed in gapped phases[8,11]. Specifically, let us consider the following 1D **k**-space Hamiltonian corresponding to a lattice model,

$$H(k) = \sigma_3 \cos k + i\sigma_2 \sin k + v\sigma_0 \cos(k+a) \tag{6}$$

where σ_0 is the 2×2 identity matrix. The Hamiltonian includes a term proportional to σ_0, which is useful in tuning gaps in projection bands to identify edge states. As can be commonly understood, introducing the identity term does not change the topology of the system and, in particular, the degeneracy features remain. Comparing Eq. (6) to Eq. (1), with **k**-space represented by a 1D momentum k, we obtain the following correspondence: $f_3(k) = \cos k$ and $f_2(k) = \sin k$. The path traced out by $(f_2(k), f_3(k))$ goes around the NIP as shown in Fig. 4a, and we can see that the 1D Brillouin zone of the lattice model carries the topological invariant Z_1Z_3 (cf. Fig. 2d). Such a Hamiltonian can be experimentally realized by the 1D tight-binding lattice as shown in Fig. 4b. To observe the topological edge states, we need to consider the band structure and topology of the systems with open boundary condition (OBC) and periodic boundary condition (PBC), respectively. The schematic sample with finite number of unit cells under PBC is shown in the upper panel of Fig. 4b, in which the terminal unit cells are connected via the hoppings. The sample under OBC is shown in the lower panel of Fig. 4b, where the terminal unit cells are disconnected. The corresponding real-space Hamiltonian is

$$H_r = \underbrace{\frac{1}{2}(\sigma_3 + \sigma_2 + ve^{ia}\sigma_0)}_{\hat{t}_1} \sum_j c_j^\dagger c_{j+1} + \underbrace{\frac{1}{2}(\sigma_3 - \sigma_2 + ve^{-ia}\sigma_0)}_{\hat{t}_2} \sum_j c_j^\dagger c_{j-1} \tag{7}$$

where j denotes unit cell index. The hopping of orbitals is described by two 2×2 hopping matrices $\hat{t}_1$ and $\hat{t}_2$, whose entries represent the hopping parameters between lattice sites, as shown in Fig. 4c. The hopping matrices satisfy the relation $\hat{t}_1^* = \hat{t}_2$. As can be seen from Eq. (7), the intercell hoppings between adjacent unit cells are non-Hermitian and nonreciprocal, meaning that the two directional hopping matrices $\hat{t}_1 \neq \hat{t}_2^{\dagger}$. Rather, they have entries that are negatively conjugate to each other $t_1^{12} = -(t_2^{21})^*$ **Error! Bookmark not defined.** and $t_1^{21} = -(t_1^{12})^*$. Such tight-binding models can potentially be realized by electric circuits and phononic lattices incorporating active devices[41,52]. As the 1D Brillouin zone inevitably cuts through the ELs four times, the band structure undergoes line-gap closing four times, as shown in Fig. 4d. Clearly, the conventional Zak phase, which is commonly used for explaining edge states in gapped 1D systems, cannot be defined in this 1D Brillouin zone. Nevertheless, the two eigenstates experience frame deformation process along each path, evolving from parallel states to antiparallel states (Fig. S3b2 in Supplementary Information). This process shows that the relative rotation angle between the two eigenstates is π, which equals an integral

$$\psi = \oint_{l_\alpha} i \langle \varphi | \nabla_k \varphi \rangle dk \tag{8}$$

The loop l_α of the integration [Eq. (8)] is shown in Fig. 4e and connects the trajectories of the two eigenvalues along the path α at the ELs. In this context, the loop l_α is in the 3D Re(E)-f_2-f_3 space. Moreover, Eq. (8) represents the conventional Berry phase, which is related to the frame deformation along α. Along the path α', the two eigenstates swap in comparison to α, resulting in a relative rotation angle of $-\pi$. This means that the Berry phase along the loop $l_{\alpha'}$ given by Eq. (8) is $-\pi$ (see Fig. 4d). Additionally, the identity term in the Hamiltonian [Eq. (6)] creates a real line gap between the eigenenergies on α and α' in the projection band. As a result, if we truncate the 1D system with open boundaries, there will be a pair of edge modes residing in this line gap, as shown in Fig. 4f, where the black and red dots represent the projection bands under OBC and PBC. In broken phases, the eigenenergies form point gaps in the projection band, which lead to the non-Hermitian skin effect as indicated by black dots in the continuum in Fig. 4f. It is shown that the eigenvalues of the skin modes form arcs located inside the loop of the eigenmodes under PBC on the complex plane. The edge states are separate from any bulk modes and skin modes in the continuum, making them easily distinguishable. The field distribution (amplitude $|\varphi|$) of one edge mode is shown in Fig. 4g, where clearly the field is confined at the left edge of the 1D chain (inset).

To summarize, we have topologically classified a generic non-Hermitian two-level system possessing *PT*-symmetry and an additional pseudo-Hermitian symmetry which may arise in lattice systems with nonreciprocal hopping[41,46–48]. These systems feature surfaces of exceptional points that host stable embedded intersection singularities in momentum space. Our study demonstrates that the topology of this gapless structure can be understood by examining the quotient space under equivalence relations of eigenstates, which turns out to be a bouquet of three circles. The fundamental group of this space is isomorphic to a free non-Abelian group on three generators. This classification enables us to predict the formation and evolution of chain-like structures of NILs as the Hamiltonian deforms, based on the conservation of topological invariants. Our work further leads to prediction for the existence of topologically protected edge states in 1D lattice models, which is a remarkable and counterintuitive phenomenon for such gapless phases, going beyond the conventional Zak phase understanding. The methods of quotient space topology and intersection homotopy theory might potentially be extended to systematically classify other hypersurface singularities in non-Hermitian systems, such as high-order exceptional points as cusps[32,40] and more complicated swallowtail catastrophes[41]. Our work also proposed a new kind of non-Hermitian gapless topological phase of matter, providing pathways for designing systems to realize robust topological non-defective degeneracies in non-Hermitian systems.

Acknowledgments: This work is supported by Research Grants Council of Hong Kong through grants AoE/P-502/20, 16307621, 16307821, 16310420. Y. Zhu acknowledges the financial support from National Natural Science Foundation of China grant 11701263.

Author contributions: H.J. and C.T.C. planned the project. H.J., R.Y.Z., Y.Z. constructed the theoretical framework. H.J., R.Y.Z., Y.Z. and C.T.C. wrote the manuscript. All authors contributed to the discussion.

Competing interests: The authors declare no competing interests.

Data and codes are available for this work.

Additional Information:

Supplementary Information is available for this paper.

Correspondence and requests for materials should be addressed to: zhuyf@sustech.edu.cn; phchan@ust.hk.

References:

1. Lu, L., Fu, L., Joannopoulos, J. D. et al., Weyl points and line nodes in gyroid photonic crystals, *Nat. Photon.* **7**, 294–299 (2013).

2. Lu, L., Joannopoulos, J. D., Soljačić, M., Topological photonics, *Nat. Photon.* **8**, 821–829 (2014).

3. Abanin, D. A., Morozov, S. V., Ponomarenko, L. A. et al., Giant nonlocality near the Dirac point in graphene, *Science* **332**, 328–330 (2011).

4. Jiang, Z., Zhang, Y., Stormer, H. L. et al., Quantum Hall states near the charge-neutral Dirac point in graphene, *Phys. Rev. Lett.* **99**, 106802 (2007).

5. Lu, L., Wang, Z., Ye, D. et al., Experimental observation of Weyl points, *Science* **349**, 622–624 (2015).

6. Wu, Q. S., Soluyanov, A. A., Bzdušek, T., Non-Abelian band topology in noninteracting metals, *Science* **365**, 1273–1277 (2019).

7. Yang, E., Yang, B., You, O. et al., Observation of non-Abelian nodal links in photonics, *Phys. Rev. Lett.* **125**, 033901 (2020).

8. Guo, Q., Jiang, T., Zhang, R. Y. et al., Experimental observation of non-Abelian topological charges and edge states, *Nature* **594**, 195–200 (2021).

9. Soluyanov, A. A., Gresch, D., Wang, Z. et al., Type-II Weyl semimetals, *Nature* **527**, 495–498 (2015).

10. Yang, L. X., Liu, Z. K., Sun, Y. et al., Weyl semimetal phase in the non-centrosymmetric compound TaAs, *Nat. Phys.* **11**, 728–732 (2015).

11. Yang, B., Guo, Q., Tremain, B. et al., Ideal Weyl points and helicoid surface states in artificial photonic crystal structures, *Science* **359**, 1013–1016 (2018).

12. Jia, H., Zhang, R., Gao, W. et al., Observation of chiral zero mode in inhomogeneous three-dimensional Weyl metamaterials, *Science* **363**, 148–151 (2019).

13. Jia, H., Zhang, R. Y., Gao, W. et al., Chiral transport of pseudospinors induced by synthetic gravitational field in photonic Weyl metamaterials, *Phys. Rev. B* **104**, 045132 (2021).

14. Gong, Z., Ashida, Y., Kawabata, K. et al., Topological phases of non-Hermitian systems, *Phys. Rev. X* **8**, 031079 (2018).

15. Yao, S., Wang, Z., Edge states and topological invariants of non-Hermitian systems, *Phys. Rev. Lett.* **121**, 086803 (2018).

16. Shen, H., Zhen, B., Fu, L., Topological band theory for non-Hermitian Hamiltonians, *Phys. Rev. Lett.* **120**, 146402 (2018).

17. Okuma, N., Kawabata, K., Shiozaki K. et al., Topological origin of non-Hermitian skin effects, *Phys. Rev. Lett.* **124**, 086801 (2020).

18. Leykam, D., Bliokh, K. Y., Huang, C. et al., Edge modes, degeneracies, and topological numbers in non-Hermitian systems, *Phys. Rev. Lett.* **118**, 040401 (2017).

19. Bergholtz, E. J., Budich, J. C., Kunst, F. K., Exceptional topology of non-Hermitian systems, *Rev. Mod. Phys.* **93**, 015005 (2021).

20. Kawabata, K., Shiozaki, K., Ueda, M. et al., Symmetry and topology in non-Hermitian physics, *Phys. Rev. X* **9**, 041015 (2019).

21. Borgnia, D. S., Kruchkov, A. J., Slager, R. J., Non-Hermitian boundary modes and topology, *Phys. Rev. Lett.* **124**, 056802 (2020).

22. Kawabata, K., Bessho, T., Sato, M., Classification of exceptional points and non-Hermitian topological semimetals, *Phys. Rev. Lett.* **123**, 066405 (2019).

23. Song, F., Yao, S., Wang, Z., Non-Hermitian topological invariants in real space, *Phys. Rev. Lett.* **123**, 246801 (2019).

24. Zhou, H., Peng, C., Yoon, Y. et al., Observation of bulk Fermi arc and polarization half charge from paired exceptional points, *Science* **359**, 1009–1012 (2018).

25. Helbig, T., Hofmann, T., Imhof, S. et al., Generalized bulk–boundary correspondence in non-Hermitian topolectrical circuits, *Nat. Phys.* **16**, 747–750 (2020).

26. Wang, K., Dutt, A., Wojcik, C. C. et al., Topological complex-energy braiding of non-Hermitian bands, *Nature* **598**, 59–64 (2021).

27. Zhou, H, Lee, J. Y., Liu, S. et al., Exceptional surfaces in PT-symmetric non-Hermitian photonic systems, *Optica* **6**, 190–193 (2019).

28. Okugawa, R., Yokoyama, T., Topological exceptional surfaces in non-Hermitian systems with parity-time and parity-particle-hole symmetries, *Phys. Rev. B* **99**, 041202 (2019).

29. Zhang, X., Ding, K., Zhou, X. et al., Experimental observation of an exceptional surface in synthetic dimensions with magnon polaritons. *Phys. Rev. Lett.* **123**, 237202 (2019).

30. Yang, Z., Hu, J., Non-Hermitian Hopf-link exceptional line semimetals, *Phys. Rev. B* **99**, 081102 (2019).

31. Zhong, Q., Ren, J., Khajavikhan, M. et al., Sensing with exceptional surfaces in order to combine sensitivity with robustness, *Phys. Rev. Lett.* **122**, 153902 (2019).

32. Tang, W., Jiang, X., Ding, K. et al., Exceptional nexus with a hybrid topological invariant. *Science* **370**, 1077–1080 (2020).

33. Wojcik, C. C., Sun, X. Q., Bzdušek, T. et al., Homotopy characterization of non-Hermitian Hamiltonians, *Phys. Rev. B* **101**, 205417 (2020).

34. Sun, X. Q., Wojcik, C. C., Fan, S. et al., Alice strings in non-Hermitian systems, *Phys. Rev. Res.* **2**, 023226 (2020).

35. Li, Z., Mong, R. S. K., Homotopical characterization of non-Hermitian band structures, *Phys. Rev. B* **103**, 155129 (2021).

36. Soleymani, S., Zhong, Q., Mokim, M. et al., Chiral and degenerate perfect absorption on exceptional surfaces. Nat. Commun. **13**, 599 (2022).

37. Xiao, Y. X., Ding, K., Zhang, R. Y. et al., Exceptional points make an astroid in non-Hermitian Lieb lattice: Evolution and topological protection, *Phys. Rev. B* **102**, 245144 (2020).

38. Sayyad, S., Stalhammar, M., Rodland, L. et al., Symmetry-protected exceptional and nodal points in non-Hermitian systems, arXiv preprint arXiv:2204.13945, 2022.

39. Zhang, R. Y., Cui, X., Chen, W. J. et al., Symmetry-protected topological exceptional chains in non-Hermitian crystals, arXiv preprint arXiv:2204.08052, 2022.

40. Delplace, P., Yoshida, T., Hatsugai, Y., Symmetry-protected multifold exceptional points and their topological characterization, *Phys. Rev. Lett.* **127**, 186602 (2021).

41. Hu, J., Zhang, R. Y. et al., Non-Hermitian swallowtail catastrophe revealing transitions among diverse topological singularities, DOI: 10.1038/s41567-023-02048-w, accepted for publication in *Nat. Phys.* (2023).

42. Mostafazadeh, A., Pseudo-Hermitian representation of quantum mechanics, *Int. J. Geo. Meth. Mod. Phys.* **7**, 1191–1306 (2010).

43. Mostafazadeh, A., Quantum brachistochrone problem and the geometry of the state space in pseudo-Hermitian quantum mechanics, *Phys. Rev. Lett.* **99**, 130502 (2007).

44. Freedman, D. Z., Van Proeyen, A., Supergravity, Cambridge University Press, 2012.

45. Frankel, T., The geometry of physics: An introduction, Cambridge University Press, 2011.

46. Buddhiraju, S., Song, A., Papadakis, G. T. et al., Nonreciprocal metamaterial obeying time-reversal symmetry, *Phys. Rev. Lett.* **124**, 257403 (2020).

47. Wang, X., Ptitcyn, G., Asadchy, V. S. et al., Nonreciprocity in bianisotropic systems with uniform time modulation, *Phys. Rev. Lett.* **125**, 266102 (2020).

48. Ezawa, M., Non-Hermitian non-Abelian topological insulators with PT symmetry, *Phys. Rev. Res.* **3**, 043006 (2021).

49. Spanier, E. H., Algebraic topology, Springer Science & Business Media, 1989.

50. Gajer, P., The intersection Dold-Thom theorem, *Topology* **35**, 939–967 (1996).

51. Kirwan, F., Woolf, J., An introduction to intersection homology theory (2nd edition), Chapman and Hall/CRC, 2006.

52. Zhang L., Yang Y., Ge Y., et al. Acoustic non-Hermitian skin effect from twisted winding topology, *Nat. Commun.* **12**, 6297 (2021).

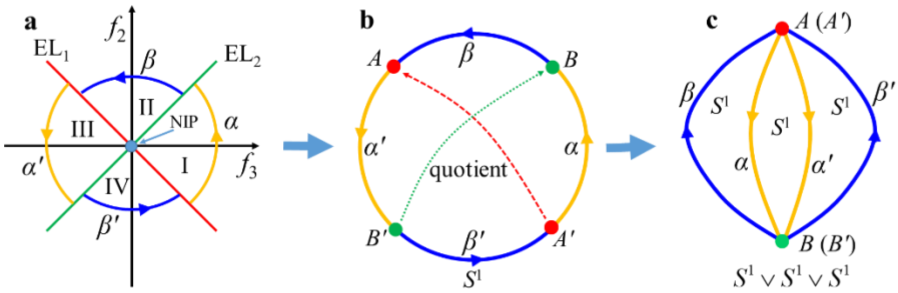

Fig. 1| Construction of a quotient space under equivalence relations. a The gapless structure of the order-parameter space (i.e. $f_{2,3}$ plane), where EL_1 and EL_2 are exceptional lines satisfying $f_2 = \mp f_3$, respectively. The NIP is at the origin where the ELs intersect, with $f_2 = f_3 = 0$.. Regions I and III are *PT*-exact phases, and Regions II and IV are *PT*-broken phases. **b** The 2D plane excluding the NIP can deformation retract to a circle S^1, with the upper and lower parts of EL_1 shrinking to A and A', respectively, and with those of EL_2 to B and B'. **c** Gluing identified points A with A', and B with B', we obtain the quotient space of S^1 in panel **b** as a bouquet of three circles.

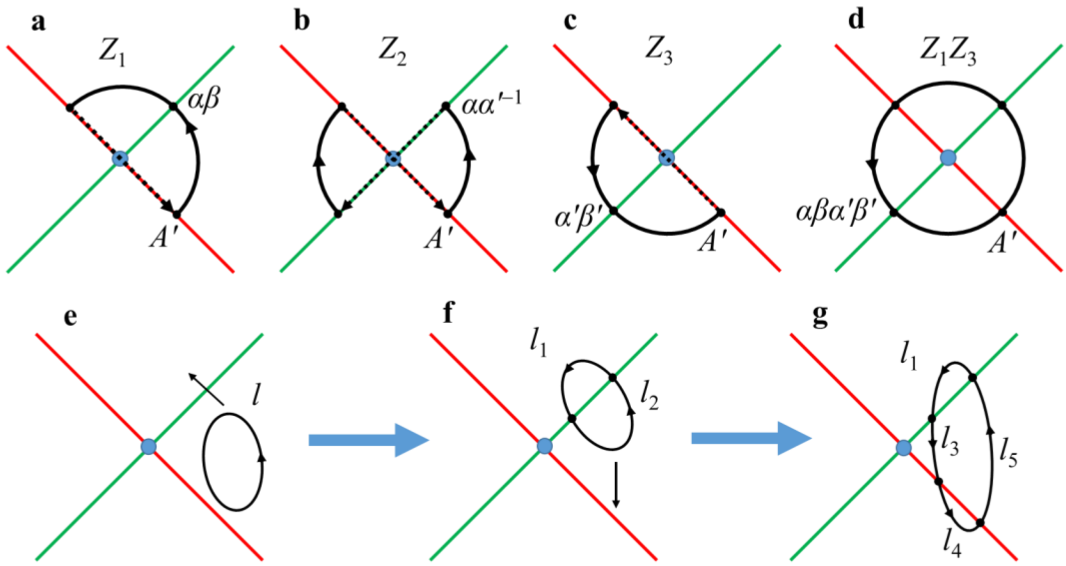

Fig. 2| Typical loops carrying nontrivial or trivial topological invariants. a–c Loops carrying nontrivial topological invariants Z_1, Z_2 and Z_3, respectively, which are the generators of the group [Eq. (4)]. The dashed lines with arrow denote quotient maps, i.e., gluing of identified points. **d** The loop formed by the concatenation $\alpha\beta\alpha'\beta'$ encloses the NIP, which carries the topological invariant Z_1Z_3. Point A' in panels **a–d** denotes the basepoint. **e–g** Evolution of a loop carrying trivial topological charge. **e** A loop without touching ELs is confined within a specific region and is trivial. **f** Moving the loop l in panel **e** upwards along the black arrow direction, we see that it becomes a product of paths l_1 and l_2. Both l_1 and l_2 are trivial loops in the quotient space M, and thus the loop as their product is also trivial. **g** Stretching the loop along the black arrow direction in panel **f**, we obtain that the loop crosses EL_1 and becomes a product $l_1l_3l_4l_5$ of paths. The path l_4, similar to l_1 and l_2, corresponds to a trivial loop in the quotient space M. The paths l_5 and l_3 are oriented in opposite directions (labeled by the arrows) and are homotopic to α and α^{-1}, respectively (cf. Fig. 1a). The path product $l_1l_3l_4l_5$ is thus trivial.

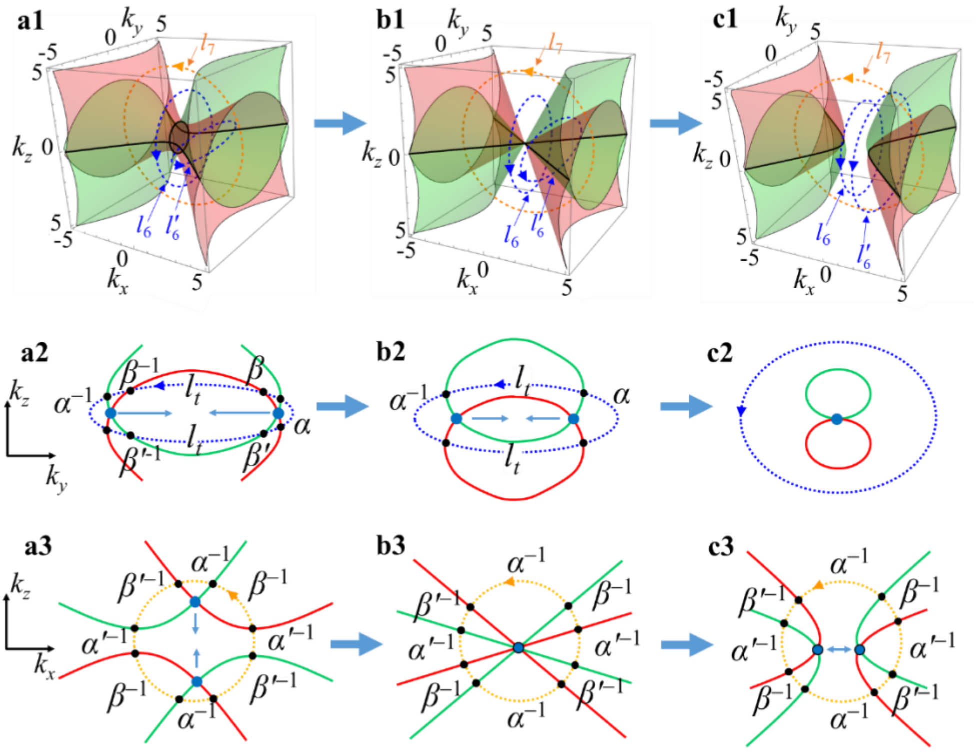

Fig. 3| Explaining the formation of the chain of NILs in k-space and its evolution against perturbations with the fundamental group. a1–c1 ESs (red and green surfaces) and NILs (black lines) plotted from Eq. (5), with $d > 0$, $d = 0$ and $d < 0$, respectively. The blue loops l_6 and l_6' have trivial topological invariants. **a2–c2** Cross sections on the plane containing l_6'. The enclosed pair of NILs can annihilate each other. Each path l_t is a path with its endpoints on the same ES without cutting through the other ES. Similar to l_1, l_2 and l_4 in Fig. 2, l_t carries a trivial topological invariant (the subscript t stands for "trivial"). **a3–c3** Cross sections on the plane containing the orange loop l_7. The NILs enclosed cannot annihilate each other. Red and green lines: ESs; Dark blue dots: NILs; Black dots: intersecting points of loops with ESs (in both Row 2 and Row 3).

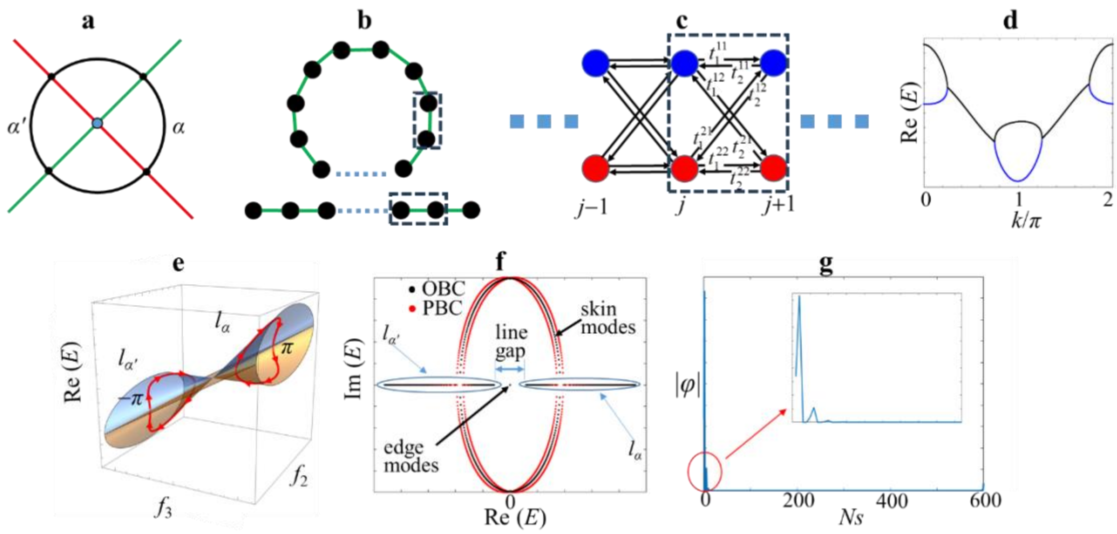

Fig. 4| Topologically protected edge states by the invariant Z_1Z_3. a A loop circulating the NIP, as the Brillouin zone of the 1D lattice model in Eq. (6), is partitioned into four paths, with α and α' residing in exact phases. **b**. Sample designs of the lattice model under PBC (upper panel, terminal unit cells are connected with hoppings) and OBC (lower panel, terminal unit cells are disconnected). Here the black circles denote unit cells and the green bonds denote the hopping matrices connecting adjacent unit cells. The dashed blocks encircle two unit cells, and the structure inside the block is shown in panel **c**. **c** Realization of the lattice model. The dashed block shows the internal structure of unit cells and the hoppings (labelled in panel **b** with dashed blocks). The hopping parameters $t_{1,2}^{11}$, $t_{1,2}^{12}$, $t_{1,2}^{21}$ and $t_{1,2}^{22}$ are the entries of the hopping matrices $\hat{t}_1$ or $\hat{t}_2$ in Eq. (7). **d** Eigenvalue dispersions (real part) of the model of Eq. (7) in the 1D Brillouin zone. Since the Brillouin zone cuts through ELs four times, the band structure experience gap closing four times. **e** Joining the trajectories of two bands on the path α forms a loop in Re(E)-f_2-f_3 space l_α, along which the Berry phase is π. This quantized Berry phase is equal to the relative rotation angle between the two eigenstates resulting from frame deformation along α. For the path α', joining the two bands forms the loop $l_{\alpha'}$, along which the Berry phase is $-\pi$. This is because from α to α' the two eigenstates swap due to band inversion at NIP. The relative rotation angle between the eigenstates changes sign. **f** Plots of projection bands of the 1D lattice model under open boundary condition (OBC, black dots) and periodic boundary condition (PBC, red dots). There exists a pair of edge modes in the line gap for eigenstates along the loops l_α and $l_{\alpha'}$ in panel **e**. **g** Field distribution of one edge mode. The lattice model with OBC has 300 periods (600 lattice sites, denoted by *Ns*). Inset: zoom-in view showing the field distribution near the left edge.

Supplementary Information: Topological classification for intersection singularities of exceptional surfaces in pseudo-Hermitian systems

Hongwei Jia[#], Ruo-Yang Zhang[#], Jing Hu, Yixin Xiao, Shuang Zhang, Yifei Zhu[*], C. T. Chan[†]

1. Pseudo-Hermiticity and metric operator

The pseudo-Hermiticity can be regarded as a symmetry in non-Hermitian physics[1], and a formal definition of pseudo-Hermiticity is always accompanied with a metric operator η

$$\eta H \eta^{-1} = H^{\dagger} \tag{S1}$$

Hence, a pseudo-Hermitian system is also called a η-pseudo-Hermitian system, and the metric operator η is a Hermitian matrix. Recently, the parity-time inversion symmetry (*PT*) is included in pseudo-Hermiticity symmetry[2,3]. The considered system thus includes two inequivalent pseudo-Hermitian symmetries. In quantum mechanics, the Hamiltonians of two systems can be considered to be equivalent if they can transform to each other via unitary transformations ($U^{-1} = U^{\dagger}$)

$$H\varphi = E\varphi \to UHU^{\dagger}U\varphi = EU\varphi \to H'\varphi' = E\varphi' \tag{S2}$$

We apply the transformation to Eq. S1

$$\begin{aligned} &U\eta H \eta^{-1} U^{\dagger} = UH^{\dagger}U^{\dagger} \\ &\to U\eta U^{\dagger} UHU^{\dagger} U\eta^{-1}U^{\dagger} = UH^{\dagger}U^{\dagger} \\ &\to \eta' H' \eta'^{-1} = H'^{\dagger} \end{aligned} \tag{S3}$$

where $\eta' = U\eta U^{\dagger}$ is the transformed metric operator. For the considered system in Eq. (S2), one can apply an SU(2) transformation to the Hamiltonian, e.g.

$$\begin{aligned} H' &= e^{i\frac{\theta}{2}\sigma_1} H e^{-i\frac{\theta}{2}\sigma_1} \\ &= (f_2(\mathbf{k}) i\sigma_2 + f_3(\mathbf{k})\sigma_3)\cos\theta + (-f_2(\mathbf{k}) i\sigma_3 + f_3(\mathbf{k})\sigma_2)\sin\theta \end{aligned} \tag{S4}$$

It is found that the Hamiltonian can be transformed to a PT-symmetric system with equal gain and loss for $\theta = \pi / 2$,

$$H' = -f_2(\mathbf{k}) i\sigma_3 + f_3(\mathbf{k})\sigma_2 \quad \text{(S5)}$$

and the metric operator is simultaneously transformed to

$$\eta' = \begin{bmatrix} 0 & i \\ -i & 0 \end{bmatrix} \quad \text{(S6)}$$

Hence, the classification in this work can be extended to other PT-symmetric pseudo-Hermitian systems (e.g. realized by equal gain and loss, Eq. S5) with equivalent metric operators[4].

2. Quotient space and stratified space

In topology, the quotient space of a topological space under given equivalence relations is a new topological space constructed by endowing the quotient set of the original topological space with the quotient topology[5]. Let (X, τ_X) be a topological space, and let ~ be equivalent relation on X. The quotient set $Y=X/\sim$ is the set of equivalence classes of elements of X. The equivalence class of $x \in X$ is denoted by $[x]$. The quotient map associated with ~ refers to the surjective map

$$\begin{aligned} q : X &\to X / \sim \\ x &\to [x] \end{aligned} \quad \text{(S7)}$$

Intuitively speaking, all points in each equivalence class are identified or glued together. A well-known example of quotient space is the Brillouin zone. In the momentum space of periodic systems, a point $\mathbf{k}$ is identified with points $\mathbf{k}+m_a\mathbf{G}_a$ because a $\mathbf{k}$-space Hamiltonian at these points have the same eigenvalues and eigenstates. Here $\mathbf{G}_a$ are reciprocal lattice vectors and m_a are integers. That is why we mostly considers the band dispersions in the first Brillouin zone. It is also notable that the points on one side of the Brillouin zone boundaries can be translated to the points on the other boundary under translational operations of $\mathbf{G}_a$. Such points are identified and can be glued together. As simple examples, the first Brillouin zone is a quotient map of the momentum space under equivalence relation of translations by $\mathbf{G}_a$, and points in the first Brillouin zone are the representatives of all the equivalence classes. For 1D periodic systems, identifying points on the first Brillouin zone boundary constructs a quotient space, which is a 1D circle S^1 (see Fig. S1a1-a2). Similarly, opposite edges (p_1 and p_2, and p_3 and p_4) of the Brillouin zone of 2D periodic systems can be identified (see Fig. S1b1). By gluing p_1 to p_2, the Brillouin zone becomes a cylinder (see Fig. S1b2). We further glue p_3 to p_4, and the cylinder becomes a torus T (see Fig. S1b3). p_1 (or p_2) and p_3 (or p_4) are called the skeleton of the torus, and is a bouquet of two circles with a common basepoint $S^1 \vee S^1$. The surface of the torus is called the two-cell. Assembling the skeleton and the two-cell, the torus can be described by the product $T = S^1 \times S^1$. The topology of the torus is thus described by its fundamental group $\pi_1(T) = \mathbf{Z} \times \mathbf{Z}$. This is a free Abelian group on two generators.

The momentum space of the considered system is a stratified space[6,7]. In topology, a stratified space is a triple (V,S,ζ), where V is a topological space (often we require it to be locally compact, Hausdorff, and second countable), S is a decomposition of V into strata $V = \bigcup_{X \in S} X$, and ζ is the set of control data $\{(T_X),(\pi_X),(\rho_X)|X \in S\}$, where T_X is an open neighborhood of the stratum X, π_X: $T_X \rightarrow X$ is a continuous retraction, and ρ_X: $T_X \rightarrow [0,+\infty)$ is a continuous function. These data need to satisfy the following conditions:

1. Each stratum X is a locally closed subset and the decomposition S is locally finite.

2. The decomposition S satisfies the axiom of the frontier: if X, $Y \in S$ and $Y \cap \bar{X} \neq \varnothing$, then $Y \subset \bar{X}$. The condition implies that there is a partial order among strata: $Y<X$ if and only if $Y \subset \bar{X}$ and $Y \neq X$.

3. Each T_X is a smooth manifold.

4. $X=\{v \in T_X|\, \rho_X(v)=0\}$. So ρ_X can be viewed as the distance function from the stratum X.

5. For each pair of strata $Y<X$, the restriction (π_X, ρ_X): $T_Y \cap X \rightarrow Y \times (0,+\infty)$ is a submersion.

6. For each pair of strata $Y<X$, there holds $\pi_Y \circ \pi_X = \pi_Y$ and $\rho_Y \circ \pi_X = \rho_Y$.

Consider the parameter space f_2-f_3 of our Hamiltonian, the topological space V is simply the plane (Fig. S2). Thus S is the decomposition of V into three strata (X, Y, Z), which are the 2D space R^2 (X), the singular hypersurfaces ELs at $f_2 = \pm f_3$ (Y=Sing(X)), and the hypersurface singularity NIP (Z=Sing(Sing(X))) at the center, as shown in Fig. S2. For each stratum (e.g. X), the smooth manifold T_X considers the nearby neighborhood. Therefore, T_1-T_3 in Fig. S2 correspond to the three strata X, Y and Z, respectively.

Our classification is based on eigenstates. The Hamiltonian in spaces without gap closing can be expressed with the sum

$$H = \sum_{i=1,2} E_i \left|\varphi_i^L\right\rangle\left\langle\varphi_i^R\right| \tag{S8}$$

where $\varphi_i^{L(R)}$ denote the left and right eigenstates of the Hamiltonian. The pseudo-Hermiticity and PT symmetries of the system enforces the left and right eigenstates (both in exact and broken phases) to be connected by the following relation

$$\varphi_i^L = \eta(\varphi_i^R)^* \tag{S9}$$

The quotient space is constructed by identifying points with the same eigenstates. Note that the eigenstates are ordered by the corresponding eigenvalues, and the criterion for ordering eigenstates has been introduced in the main text. Hence, gluing point A' and point A, and B to B' is understandable, because the two eigenstates at these points coalesce, and ordering eigenstates is meaningless at these points.

$$\begin{aligned} \varphi_1 = \varphi_2 &= \begin{bmatrix} -1 \\ 1 \end{bmatrix} \quad for \;\; f_2 = f_3 \\ \varphi_1 = \varphi_2 &= \begin{bmatrix} 1 \\ 1 \end{bmatrix} \quad for \;\; f_2 = -f_3 \end{aligned} \tag{S10}$$

However, in spaces without gap closing, by adding a minus sign to the Hamiltonian in Eq. S8, both eigenenergies take negative signs, and the eigenstates remain the same. This process can be realized by taking the negatives of f_2 and f_3, which are just the antipodal points lying in opposite regions with respect to the NIP. Even though the two points have the same eigenstates, the order of the two states exchanges for antipodal points because eigenvalues are added by minus signs. Therefore, the two points cannot be identified, which is distinct from the points on ELs. The constructed space Eq. (3) in the main text is a stratified quotient space, and the corresponding topology Eq. (4) is thus a quotient space topology. Since the nontrivial loops in parameter (or quotient) space all traverses the singular hypersurfaces (i.e. EL or ES), our approach is affiliated to the intersection homotopy theory[6].

3. Frame deformation of eigenstates

The metric operator for pseudo-Hermiticity plays a similar role as the space-time metric in general relativity[8,9], and the eigenstates are like local coordinate frames (or tetrad). The local metric g can be defined with the indefinite inner product $g_{mn} = \langle \varphi_m | \eta\varphi_n \rangle$ [10]. In our previous work discussing the topology of swallowtail catastrophes in non-Hermitian systems[10], we established the relationship between the local metric g and the geometric phase. Here we repeat the derivation details. The evolution problem is governed by the equation

$$H|\varphi_m\rangle = i\partial_\zeta |\varphi_m\rangle \tag{S11}$$

where ζ denotes a path parameter, and φ_m are the eigenstates. The completeness of eigenstates (off ES) shows that any field can be expanded as

$$\phi_n(\lambda(\zeta)) = \sum_m [U(\lambda(\zeta))]^{-1}{}_n{}^m \varphi_m(\lambda(\zeta)) \tag{S12}$$

where λ denotes the parameter space of the Hamiltonian with components $\lambda^1, \lambda^2, \lambda^3 \ldots$. It is not difficult to find that ϕ_n is also the solution of Eq. S11. In static evolution problems, $\phi_n(\lambda(\zeta))$ represents $\varphi_n(\lambda(\zeta+\delta\zeta))$. Applying the partial derivative with respect to ζ, one obtains

$$
\begin{aligned}
i\frac{\partial}{\partial\zeta}\phi_n(\lambda(\zeta)) &= H[U(\lambda(\zeta))]^{-1}{}_n{}^m\varphi_m(\lambda(\zeta)) \\
&= i\frac{\partial[U(\lambda(\zeta))]^{-1}{}_n{}^m}{\partial\zeta}\varphi_m(\lambda(\zeta)) + i[U(\lambda(\zeta))]^{-1}{}_n{}^m\frac{\partial\varphi_m(\lambda(\zeta))}{\partial\zeta}
\end{aligned} \tag{S13}
$$

The instantaneous eigenvalue problem

$$
H(\lambda(\zeta))\varphi_m(\lambda(\zeta)) = E_m\varphi_m(\lambda(\zeta)) \tag{S14}
$$

and applying a scalar product by the left eigenstate $\langle\varphi_l'|$ from the left of Eq. S13 yields

$$
-iE_l[U(\lambda(\zeta))]^{-1}{}_n{}^l = \frac{\partial[U(\lambda(\zeta))]^{-1}{}_n{}^l}{\partial\zeta} + \langle\varphi_l'|\frac{\partial|\varphi_m(\lambda(\zeta))\rangle}{\partial\zeta}[U(\lambda(\zeta))]^{-1}{}_n{}^m \tag{S15}
$$

The partial derivative with respect to ζ can be expanded as

$$
\frac{\partial|\varphi_m(\lambda(\zeta))\rangle}{\partial\zeta} = \sum_k\frac{\partial|\varphi_m(\lambda(\zeta))\rangle}{\partial\lambda^k}\frac{\partial\lambda^k}{\partial\zeta}, \quad (k=1,2,3...) \tag{S16}
$$

We define the affine connection

$$
A_k{}^n{}_m = -\langle\varphi_n'|\frac{\partial|\varphi_m(\lambda(\zeta))\rangle}{\partial\lambda^k} = -\langle\varphi_n'|\frac{\partial}{\partial\lambda^k}|\varphi_m\rangle \tag{S17}
$$

and the solution to U^{-1} is thus obtained as

$$
U^{-1} = \mathrm{P}\exp[\int_0^\zeta ds\frac{\partial\lambda^k}{\partial s}A_k - i\int_0^\zeta dsE(\lambda(s))] = \mathrm{P}\exp(\int_{\lambda(0)}^{\lambda(\zeta)}d\lambda^k A_k)\times\exp[-i\int_0^\zeta dsE(\lambda(s))] \tag{S18}
$$

Ignoring the dynamical phase, the geometric phase is simply

$$
U^{-1} = \mathrm{P}\exp(\int_{\lambda(0)}^{\lambda(\zeta)}d\lambda^k A_k) \tag{S19}
$$

where P denotes path ordering operator, which is important here, because the affine connection A is a matrix. Considering the non-commutative nature of matrix product, A is a non-Abelian parallel transport gauge, and the integration of A on closed loops depends on the path circulating singularities. Here we define a local metric g with its elements being

$$g_{mn} = \left\langle \varphi_m \mid \eta \varphi_n \right\rangle \tag{S20}$$

which has explicit relations with the affine connection. The symmetries (Eq. 1 in the main text) of the Hamiltonian provide an important relation between the left and right eigenstates

$$\varphi'_m = \varphi_m^T \eta \text{ (or equivalently, } \varphi_m'^T = \eta \varphi_m \text{, } \left\langle \varphi'_m \right| = \left\langle \varphi_m^* \right| \eta \text{ , } \left| \varphi'_m \right\rangle = \eta \left| \varphi_m^* \right\rangle \text{)} \tag{S21}$$

This relation provides an orthogonality to the right eigenstates

$$\varphi_m^T \eta \varphi_n \begin{cases} = 0 & m \neq n \\ \neq 0 & m = n \end{cases} \tag{S22}$$

The orthogonal relation shows that the arbitrary phase can always be removed by normalizing the eigenstates (up to an unfixed sign)

$$\varphi_m \to \frac{\varphi_m}{\sqrt{\varphi_m^T \eta \varphi_m}} \tag{S23}$$

The normalization of eigenstates can make g a constant matrix and thus the partial derivative with respect to the path parameter vanishes

$$0 = \partial_\zeta g_{mn} = \partial_\zeta \left\langle \varphi_m \mid \eta \varphi_n \right\rangle \tag{S24}$$

Inserting the identity operator $I = \sum_l \left| \varphi'_l \right\rangle \left\langle \varphi_l \right| = \sum_l \left| \varphi_l \right\rangle \left\langle \varphi'_l \right|$, one obtains

$$\partial_{\lambda_k} \left\langle \varphi_m \mid \eta \varphi_n \right\rangle = \sum_l \left\langle \partial_{\lambda_k} \varphi_m \mid \varphi'_l \right\rangle \left\langle \varphi_l \middle| \eta \varphi_n \right\rangle + \sum_l \left\langle \varphi_m \mid \eta \middle| \varphi_l \right\rangle \left\langle \varphi'_l \middle| \partial_{\lambda_k} \varphi_n \right\rangle \tag{S25}$$

We note that

$$\left\langle \partial_{\lambda_k} \varphi_m \mid \varphi'_l \right\rangle = \left\langle \partial_{\lambda_k} \varphi_m \mid \eta \varphi_l^* \right\rangle = \left\langle \varphi_l^* \mid \eta \mid \partial_{\lambda_k} \varphi_m \right\rangle^* = \left\langle \varphi'_l \mid \partial_{\lambda_k} \varphi_m \right\rangle^* \tag{S26}$$

And thus relationship between the metric g and the affine connection of the geometric phase

$$A^{*\,l}_{k_i\ m} g_{ln} + g_{ml} A_{k_i\ n}^{\ l} = 0 \tag{S27}$$

This relation is important for us to predict the emergence of ELs and NIPs. More details on multiband models can be found in Ref. 10.

The local metric g is important for us to understand the evolution of eigenstates. In a specific region, g is invariant. For example in *PT*-exact phases, the local metrics in Region I and Region III are in the following forms

$$g_{\mathrm{I}} = \begin{bmatrix} 1 & 0 \\ 0 & -1 \end{bmatrix}, \quad g_{\mathrm{III}} = \begin{bmatrix} -1 & 0 \\ 0 & 1 \end{bmatrix} \tag{S28}$$

Here the sequence of eigenvalues is defined by sorting the corresponding eigenvalues from small to large. The geometric phase is an integration of the affine connection

$$U^{-1} = \mathrm{P}\exp\left(\int_{\mathbf{k}(0)}^{\mathbf{k}(\xi)} d\mathbf{k} A_{\mathbf{k}}\right) \tag{S29}$$

where P is the path ordering operator because the affine connection is a matrix. It is not difficult to find out that the two eigenstates experience Lorentz boost and the geometric phase is simply

$$U^{-1} = \exp \gamma T \tag{S30}$$

where T is the Lie algebraic generator of SO(1,1) group

$$T = \begin{bmatrix} 0 & 1 \\ 1 & 0 \end{bmatrix} \tag{S31}$$

and can be derived from Eq. (S27). Next, we define the path parameter θ (see Fig. S3a), with $f_3 = \cos\theta$ and $f_2 = \sin\theta$. The evolution of eigenvalues and eigenstates along the path α ($-\pi/4 \le \theta \le \pi/4$) is shown in Fig. S3b1 and b2, respectively. Note that the eigenstates have been rescaled. As can be indicated in Fig. S3b2, the two eigenstates are rotating in opposite directions, and resultantly, they evolve from parallel states to antiparallel states, which is typical for frame deformations. This process occurs because γ varies from $+\infty$ to 0 and to $-\infty$, and the infinity of γ is provided by the ELs, i.e. the path departs from EL_1 and terminates at EL_2. It is thus understandable that the frame deformation is a result of hyperbolic transformation, i.e. the Lorentz boost in general relativity[8]. In Region III, the evolution of eigenstates is similar to that in Region I, simply the two eigenstates swap.

In broken phases, the local metrics are both

$$g_{\text{II,IV}} = \begin{bmatrix} 0 & 1 \\ 1 & 0 \end{bmatrix}, \tag{S32}$$

and the evolution of eigenstates is still defined on SO(1,1) group. The difference is that the two eigenstates become complex conjugate, and the frame deformation process is extended to the complex space. Results for path β ($\pi/4 \le \theta \le 3\pi/4$) is provided in Fig. S3c. As shown in Fig. S3c2-c3, the initially parallel eigenstates bifurcate to form a conjugate pair, and finally evolve to two anti-parallel imaginary vectors.

With the above frame deformation process on any of the paths aforementioned, one can already determine that an NIP can be formed by the intersection of the two ELs (or ESs). Hence, an open path joining ELs (or ESs) can provide a lot of information on the intersection NIP (or NIL) of the ELs (or ESs). This is essentially different from isolated singularities, for which a path is only meaningful whenever it is closed. Therefore, if we consider a closed loop circulating a hypersurface singularity that is partitioned into several paths by the ELs (or ESs), it is necessary to investigate each open path that terminates at the ELs (or ESs) and then discuss their combinations. Our former work[10] has established the relation between the frame deformation with the conventional Berry phase, which is also mentioned in the main text to explain the topologically protected edge states.

4. Some other nontrivial loops in parameter space

In Fig. 2 of the main text, we introduced some typical nontrivial and trivial loops and the corresponding topological invariants. Since the number of elements in the group (Eq. 4) is infinitely large, and some elements other than Fig. 2 might also be useful. Here we give a brief introduction on these invariants and the corresponding path combinations in parameter space.

Figure S4a shows the path concatenation $\alpha'\beta$. Note that the basepoint has been fixed at A (or A') just like the main text, and thus we cannot exchange the order in the product (i.e. $\beta\alpha'$). Exchanging the order in the product means that the basepoint is changed from A (or A') to B (or B'). In homotopy theory, one will obtain another fundamental group by changing the basepoint without changing the order parameter space, and the groups obtained by changing the basepoint are isomorphic to each other since the quotient space M is path-connected. It is not difficult to find out that $\alpha'\beta=\alpha'\alpha^{-1}\alpha\beta$, and thus the corresponding topological invariant is $Z_2^{-1}Z_1$, which is an element of the fundamental group (Eq. 4). The path concatenation $\beta'^{-1}\beta$ is totally in broken phases, and is thus a counterpart of Fig. 2b. Since $\beta'^{-1}\beta$ can be obtained as the path product $\beta'^{-1}\alpha'^{-1}\alpha'\alpha^{-1}\alpha\beta$, it is thus obtained that the invariant on the loop is $Z_3^{-1}Z_2Z_1$. In a similar way, the path combination in Fig. S4c $\alpha\beta'$ can be obtained as the product $\alpha\alpha'^{-1}\alpha'\beta'$, and the invariant on the loop is simply $Z_2^{-1}Z_3$.

5. Non-reciprocal tight binding model realizing chain of NILs experimentally

Apart from the continuous model in the main text, the chain-like structure of NILs can also be realized with a periodic system with non-reciprocal hoppings, and such a system enables experimentally observing the chain-like structure of NILs. Here we consider a 3D fcc lattice model in Fig. S5a, and the corresponding Brillouin zone is shown in Fig. S5b, where M and N denote two inequivalent lattice sites with opposite onsite energies $\pm E_0$, respectively. The hopping between M and N (on dark green bonds) is non-reciprocal ($M\rightarrow N$: t_1, $M\rightarrow N$: $-t_1$), and the hoppings on yellow and red bonds [between the adjacent sites in the same sublattice but in different directions, i.e. yellow bonds: $\vec{r}_M \rightarrow \vec{r}_M + \vec{a} + \vec{b}$ and $\vec{r}_N \rightarrow \vec{r}_N + \vec{a} - \vec{b}$; red bonds: $\vec{r}_M \rightarrow \vec{r}_M + \vec{a} - \vec{b}$ and $\vec{r}_N \rightarrow \vec{r}_N + \vec{a} + \vec{b}$] are characterized by t_2 and $-t_2$, respectively. The corresponding real space Hamiltonian is given by

$$H_r = \sum_{\substack{\vec{r}_M \in \vec{G}_M \\ \vec{\alpha}=\vec{a},\vec{b},\vec{c}}} t_1(a^\dagger_{M,\vec{r}_M} a_{N,\vec{r}_M+\vec{\alpha}} + a^\dagger_{M,\vec{r}_M} a_{N,\vec{r}_M-\vec{\alpha}}) - h.c. + E_0(a^\dagger_{M,\vec{r}_M} a_{M,\vec{r}_M} - a^\dagger_{N,\vec{r}_N} a_{N,\vec{r}_N}) + \sum_{\substack{\vec{r}_h \in \vec{G}_h \\ h=M,N}} \mathrm{sgn}(h) t_2(a^\dagger_{h,\vec{r}_h} a_{h,\vec{r}_h+\vec{a}+\vec{b}} + h.c. - a^\dagger_{h,\vec{r}_h} a_{h,\vec{r}_h+\vec{a}-\vec{b}} - h.c.) \tag{S33}$$

where $\vec{a}$, $\vec{b}$ and $\vec{c}$ are the set of orthogonal lattice vectors connecting lattice sites M and N (see Fig. S5a). Here sgn(h)=1 and –1 for h=M and N, respectively. The corresponding **k**-space Hamiltonian can be obtained by Fourier transformation

$$\begin{aligned} H_k &= t_1(e^{ik_x} + e^{-ik_x} + e^{ik_y} + e^{-ik_y} + e^{ik_z} + e^{-ik_z}) a^\dagger_{M,k} a_{N,k} - h.c. \\ &+ E_0(a^\dagger_{M,k} a_{M,k} - a^\dagger_{N,k} a_{N,k}) \\ &+ t_2(e^{ik_x+ik_y} + e^{-ik_x-ik_y} - e^{ik_x-ik_y} - e^{-ik_x+ik_y})(a^\dagger_{M,k} a_{M,k} - a^\dagger_{N,k} a_{N,k}) \end{aligned} \tag{S34}$$

and the **k**-dependent Hamiltonian can be expressed as

$$H_1(\mathbf{k}) = \begin{bmatrix} E_0 + 2\sin k_x \sin k_y & \cos k_x + \cos k_y + \cos k_z \\ -\cos k_x - \cos k_y - \cos k_z & -E_0 - 2\sin k_x \sin k_y \end{bmatrix} \tag{S35}$$

It is can be observed that $f_3(\mathbf{k}) = E_0 + 2\sin k_x \sin k_y$ and $f_2(\mathbf{k}) = \cos k_x + \cos k_y + \cos k_z$, and thus the Hamiltonian preserves the symmetries in Eq. (1). If E_0=0, the onsite energies on M and N are the same, and the system has mirror symmetries in the x and y directions. Resultantly, the band structure is symmetric about $k_x=\pi/d_L$ and k_y=0 planes. The ESs and NILs for E_0=0 are plotted in Fig. S5c, where the red and green surfaces are ESs satisfying $f_2 = \mp f_3$, respectively. As can be seen, a chain of NILs is formed on the intersection line of the mirror planes ($k_x=\pi/d_L$ and k_y=0, see Fig. S5c). The orange dashed loop (Fig. S5d) is a combination $(\alpha'\beta'\alpha\beta)^2$ that carries a squared topological invariant $(Z_3Z_1)^2$, which means that the enclosed NILs cannot annihilate each other. The blue dashed loop does not traverse any ES and is trivial. The two loops set necessary condition for the presence of the chain of NILs. Apart from the topological invariants, the mirror symmetries is also an important factor to the emergence of chain of NILs, because the chain points are on the intersection line (red arrows) of the two mirror planes ($k_x=\pi/d_L$ and k_y=0). A nonzero E_0 can break the mirror symmetries in k_x and k_y directions, which eliminates the intersection points (as shown in Fig. S5e). However, the breaking of mirror symmetries does not affect the topology on the loops. As shown in Fig. S5e, the blue loop is still trivial, because it does not touch any ESs. The topological invariant on the orange loop is conserved [still $(Z_3Z_1)^2$], as the traversed ESs remain the same (Fig. S5d and S5f). Therefore, the emergence of the chain of NILs not only requires the symmetries in Eq. (1), but also needs two mirror symmetric planes. Such a structure is not stable against perturbations to the Hamiltonian, deforming the Hamiltonian without changing the symmetries can easily eliminate the chain of NILs as shown in Fig. 3 of the main text.

References:

1. Mostafazadeh, A., Pseudo-Hermitian representation of quantum mechanics, *Int. J. Geo. Meth. Mod. Phys.* **7**, 1191-1306 (2010).

2. Zhang, R., Qin, H., Xiao, J., PT-symmetry entails pseudo-Hermiticity regardless of diagonalizability, *J. Math. Phys.* **61**, 012101 (2020).

3. Mostafazadeh, A., Pseudo-Hermiticity versus PT-symmetry III: Equivalence of pseudo-Hermiticity and the presence of antilinear symmetries, *J. Math. Phys.* **43**, 3944-3951 (2002).

4. Özdemir, Ş. K., Rotter, S., Nori, F., et al. Parity–time symmetry and exceptional points in photonics. *Nat. Mater.* **18**, 783-798 (2019).

5. Spanier, E. H., Algebraic topology, Springer Science & Business Media, 1989.

6. Gajer, P., The intersection Dold-Thom theorem, *Topology* **35**, 939-967 (1996).

7. Kirwan, F., Woolf, J., An introduction to intersection homology theory (2nd edition), Chapman and Hall/CRC, 2006.

8. Freedman, D. Z., Van Proeyen, A., Supergravity, Cambridge university press, 2012.

9. Frankel, T., The geometry of physics: an introduction, Cambridge university press, 2011.

10. Hu, J., Zhang, R. Y. et al., Non-Hermitian swallowtail catastrophe revealing transitions among diverse topological singularities, DOI: 10.1038/s41567-023-02048-w, accepted for publication in Nat. Phys. (2023).

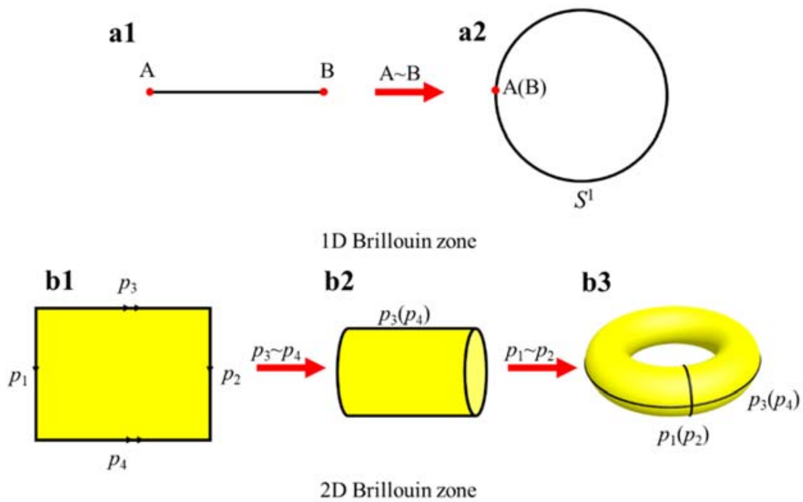

Fig. S1. Quotient space of momentum space in periodic systems. **a1-a2** The quotient space of 1D Brillouin zone is a circle (S^1) by identifying the two points on the Brillouin zone boundary. **b1-b3** Construction of quotient space of 2D Brillouin zone. Identifying the boundaries p_3 with p_4 gives a cylinder, which becomes a torus by identifying p_1 with p_2.

$$V := \mathbb{R}^2$$

$$S := \{\mathbb{R}^2, > \{|f_2| = |f_3|\}, > \{f_2 = f_3 = 0\}\}$$

$$T_1 := \mathbb{R}^2$$

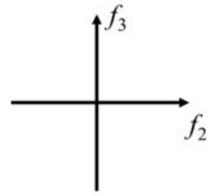

$$T_2 :=$$

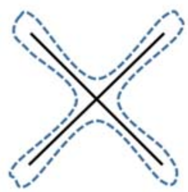

$$T_3 :=$$

Fig. S2. Stratified space of the 2D plane with ELs and NIP.

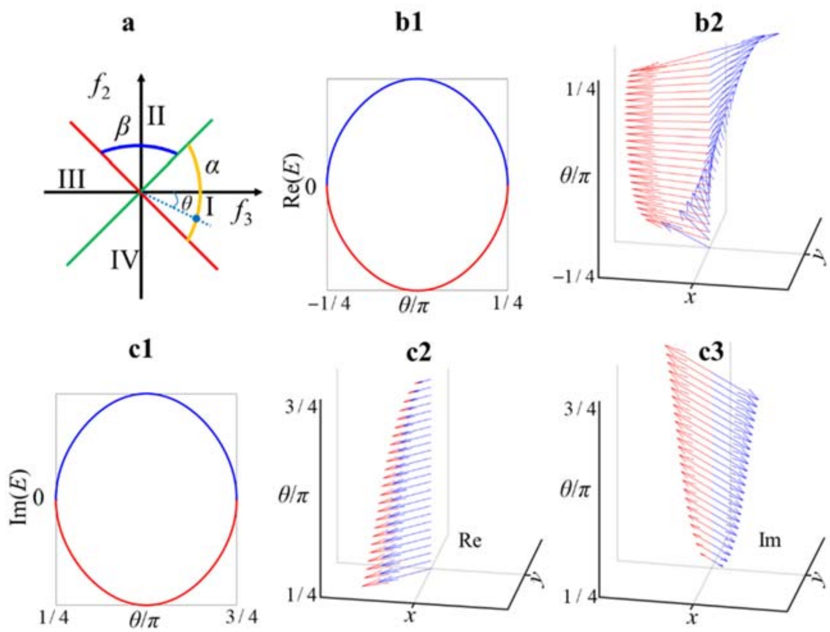

Fig. S3. Frame deformation along different paths. **a** Paths α and β in parameter space. θ denotes the path parameter, i.e. f_3=cosθ, f_2=sinθ, $-\pi/4 \le \theta \le \pi/4$ for α, $\pi/4 \le \theta \le 3\pi/4$ for β. **b1-b2** Evolution of eigenvalues (real part, see panel **b1**) and eigenstates along path α (see panel **a**). **c1-c3** Evolution of eigenvalues (imaginary part, see panel **c1**) and eigenstates (**c2**, real part; **c3**, imaginary part) along path β (see panel **a**).

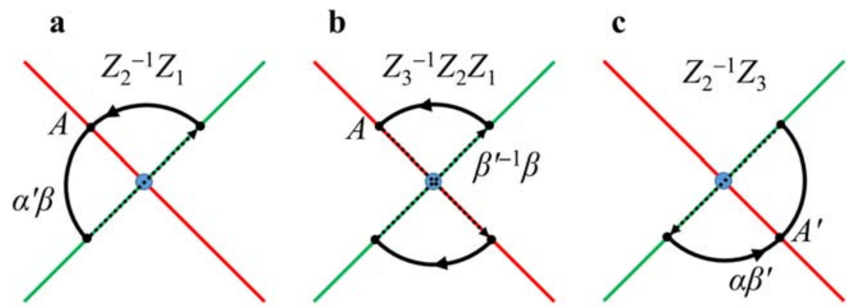

Fig. S4. Some other nontrivial loops and the corresponding topological invariants (other than Fig. 2) taking from the group Eq. 4 in the main text.

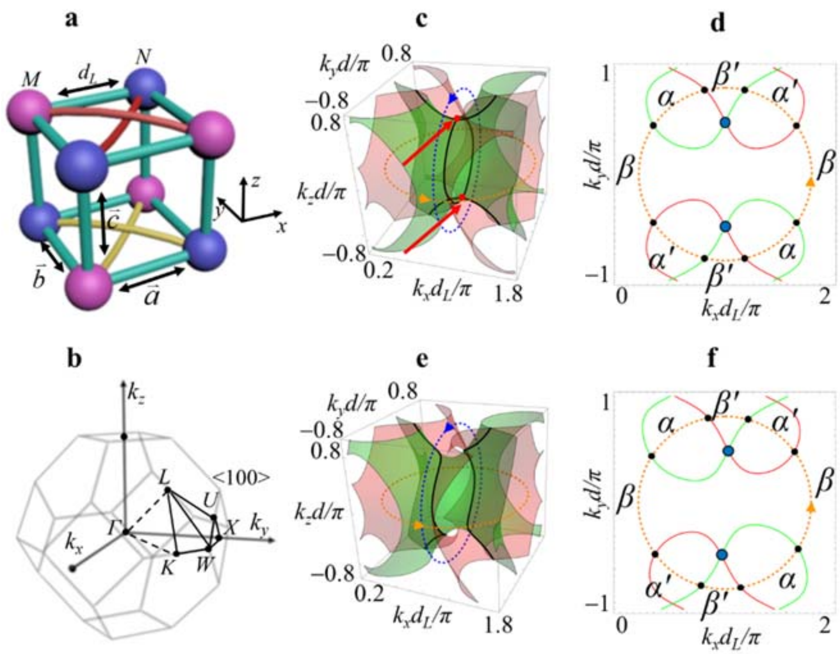

Fig. S5. Proposal of an fcc lattice model to realize the chain-like structure of NILs for experimental observation. **a** fcc lattice with two sites M (blue balls) and N (pink balls). The interspace distance between M and N is d_L, and $\vec{a}$, $\vec{b}$ and $\vec{c}$ are bond vectors. The hopping on dark green bonds is non-reciprocal ($M \to N$: t_1, $N \to M$: $-t_1$). The hopping on the same lattice sites in different directions (in $\vec{a}+\vec{b}$ and $\vec{a}-\vec{b}$) have opposite signs (hopping on yellow bonds: t_2, hopping on red bonds: $-t_2$). **b** First Brillouin zone of the fcc lattice. **c**, **e** ESs (red and green surfaces) and NILs (black lines) for E_0=0 and $E_0 \neq 0$ in Eq. (6). Panel **c** has a chain of NILs, which is symmetric with respect to <100> plane. The intersecting points on the chain are labelled with red arrows. **d**, **f** Cross section of the plane k_z=0 (where the orange loop locates) for panel **c** and panel **d**, respectively. The topological charge on the loop is conserved even though the mirror symmetries are broken.